PCCP

ARTICLE TYPE

Cite this: DOI: 00.0000/xxxxxxxxxx

Theory and Algorithms for Chiroptical Properties and Spectroscopies of Aqueous Systems

Tommaso Giovannini,[a] Franco Egidi,[b] and Chiara Cappelli *[b]

Received Date
Accepted Date

DOI: 00.0000/xxxxxxxxxx

Chiroptical properties and spectroscopies are valuable tools to study chiral molecules and assign absolute configuration. The spectra that result from chiroptical measurements may be very rich and complex, and hide much of their information content. For this reason, the interplay between experiments and calculations is especially useful, provided that all relevant physico-chemical interactions that are present in the experimental sample are accurately modelled. The inherent difficulty associated to the calculation of chiral signals of systems in aqueous solutions requires the development of specific tools, able to account for the peculiarities of water-solute interactions, and especially its ability to form hydrogen bonds. In this perspective we discuss a multiscale approach, which we have developed and challenged to model the most used chiroptical techniques.

1 Introduction

Nowadays, chiroptical properties and spectroscopies represent one of the most viable tools to study chiral molecules and assign their absolute configurations.[1–17] Different chiroptical spectroscopies offer varying insights into the physical and chemical properties of chiral systems, depending on the nature of probed signal, the peculiarities of the system, and the experimental setup.[18] The spectra that result from chiroptical measurements, however, may be very rich and complex, and hide much of their information content.[7] Special interpretative and predictive tools may therefore be highly advantageous or even outright indispensable to fully disentangle a chiroptical response, even more so than in the case of non-chiral spectroscopies.[5] To this end, ab-initio quantum-chemical simulations are especially useful as they may be applied to a very wide variety of systems and spectroscopies and yield highly accurate predictions that can be directly compared with experimental findings,[19–22] provided that all relevant physical and chemical interactions that are present in the experimental sample are also included within the theoretical model; this is especially true for the problem of correctly assigning the absolute configuration of a molecule.[4] In fact, while the absolute configuration can sometimes be worked out from the specific synthetic pathway used for the production of the system, this is not applicable in general. Chiroptical properties can readily fill this gap since two enantiomers produce chiral responses of opposite sign, which, however, must be compared with a standard of known absolute configuration. Therefore, in the absence of already available experimental data, the only way to assign the absolute configuration is to resort to the comparison between experiments and ab-initio simulations.[5,23,24] In this respect, it is crucial that the chosen computational protocol is both widely applicable and consistently reliable, since an incorrect assignment can lead to catastrophic consequences, especially if they are applied to pharmaceutical compounds.

From the theoretical point of view, chiroptical properties are rationalized in terms of a differential response exhibited by a chiral system towards polarized light. Depending on the molecular degrees of freedom that are involved in the matter-light interaction, chiral spectroscopies are usually divided into electronic or vibrational properties.[18] Examples include Electronic Circular Dichroism (ECD) and its Kramers-Kronig transform, Optical Rotation Dispersion (ORD),[18,25] belong to the first class of chiroptical properties/spectroscopies and can be understood as originating from the electronic degrees of freedom, though vibrational contributions also play a minor role.[26–33] Vibrational chiroptical spectriscopies, such as Vibrational Circular Dichroism (VCD) and Raman Optical Activity (ROA),[1–3,18,23,34–50] are instead ascribed to the vibrational domain, and as such they can provide structural information much more directly than their electronic counterparts, since they present vibrational bands which can be usually assigned to different functional groups, and are thus sensitive to the details of the molecular structure. VCD and ROA, which are collected under the umbrella of Vibrational Optical Activity methods (VOA), have demonstrated high reliability and a wide range of applicability, as it has been amply documented by a recent review.[51] Many different types of theoretical models and the corresponding computational protocols for the calculation of all mentioned chiroptical properties have been developed and presented over the years.[18,21,28,39,40,52–77] They range from

[a] Department of Chemistry, Norwegian University of Science and Technology (NTNU), 7491 Trondheim, Norway
[b] Scuola Normale Superiore, Piazza dei Cavalieri 7, I-56126 Pisa, Italy; E-mail: chiara.cappelli@sns.it

highly accurate wavefunction-based correlated ab-initio methods to approximations based on density functional theory, and their performance has been extensively evaluated.[21,64,78–85] One problem that underlies any such calculation, regardless of the chosen electronic-structure method, is the need to include a model for the interactions of the target chiral system with the molecular environment.[65]

In fact, both electronic and vibrational chiroptical spectra are usually measured in the condensed phase.[51,86–90] On one hand this is a consequence of practical experimental considerations regarding the difficulty of working with gaseous samples and the fact that the rarefied state of such systems combined with the differential nature of chiral spectroscopies would produce a signal that is almost invariably well below the detection limit. Moreover, most studied chiral molecules are in fact of biological and medical interest,[91–100] and it is therefore desirable that their spectra be measured in their natural environment, i.e. in aqueous solution.[2,51,101] It is thus crucial that a suitable quantum mechanical description of the system be coupled with a comparably accurate description of the molecular environment.[65] The difficulties inherent to the formulation of a solvation model that can successfully describe the interactions between a solute and its aqueous environment stem from the peculiarities that separate water from other common solvents.[102] Water is often considered the quintessential polar solvent. This is due to the fact that, despite its small size, it has a high molecular dipole moment. Another characteristic that separates water from other common solvents is its ability to readily form hydrogen bonds, both as donor and acceptor, giving it unique properties not shared with other solvents.[103–105] For these reasons most polar molecules are readily soluble in water, which is often referred to as the universal solvent. These two properties, i.e. high polarity and hydrogen bonding, shape the understanding most chemists have of water as a solvent. Clearly, any solvation model that seeks to describe the interaction between a solute and its aqueous environment should first and foremost accurately describe both hydrogen bonding and water's high polarity.[102] The preeminence of these two properties, however, may often overshadow other aspects which, while not as prominent, nevertheless shape the solvation phenomenon with drastic consequences, especially concerning the light-matter interaction that forms the basis for all spectroscopic phenomena.[106] One such aspect is that of solvent polarization. Water molecules in a solution do not all have the same dipole moment, rather the observed polarity is an average over all possible microscopic configurations.[107] Water molecules are polarized by the presence of other surrounding water molecules depending on their instantaneous configuration, which changes dynamically in time.[108] Keeping this in mind, when a solute is introduced into the picture, it is clear that not only can its environment have properties which may instantaneously differ from those of bulk water, but its very presence can alter the properties of the surrounding solvent molecules, depending on the solute's ability to polarize the solvent and vice versa.[109]

Chiroptical properties and spectroscopies are extremely sensitive to the solute-solvent interactions that can occur in aqueous solution, and thus to the instantaneous configuration of the system, as will be shown in the examples below.[106,110–115] For these reasons, different approaches to treat the external environment have been proposed in the last years. The most successful approaches belong to the family of the so-called focused models, in which the solute is treated at the Quantum Mechanical (QM) level, whereas the solvent is described by means of classical mechanics.[109] Such a modeling is justified by the fact that the chiroptical signal arises from the solute, whereas the achiral solvent only acts as a perturbation, and can therefore be treated at a lower level of accuracy.[22,65] The immediate advantage of this treatment is the drastic reduction in the degrees of freedom that must be accounted for, thus allowing one to treat much larger systems. It is worth noticing that in some particular cases, this type of model can fail: this can occur whenever there are chiroptical signals arising from solvent molecules themselves, which can happen whenever the solute imprints a chirality to its otherwise achiral environment. Such a phenomenon is usually called "chirality imprinting" or "chirality transfer".[111–113,116] Focused models usually ignore this phenomenon since they focus on the chiral response of the solute only, though by including water molecules into the QM layer it may be possible to describe this phenomenon.[111–113,116] Among the focused models presented over the years, the most used is the Polarizable Continuum Model (PCM),[109,117] which can produce very accurate results when applied to solvents which do not strongly interact with the solute (as for instance non-protic polar solvents), however Hydrogen Bonds (HB), which are ubiquitous in aqueous solution, cannot be properly treated.[28,118–120] Due to the unavoidably atomistic nature of HB, in order to solve such an issue, QM/Molecular Mechanics (QM/MM) approaches can be exploited because they retain the atomistic nature of the external environment.[121–123] However, the aforementioned solute-solvent mutual polarization, which is the core strength of PCM and the source of its success, can only be retained by exploiting polarizable QM/MM methods, in which the MM atoms can respond to the changes in the QM density as arising by the interaction with the polarized light.[108,124–133]

Another major difference between continuum and discrete models is that the latter can take into account the dynamical aspects of solvation. QM/PCM calculations are typically performed on minimum-energy structures which are assumed to represent the full conformational distribution of a solute in a solvent. This can only be true for rigid molecules, while for flexible systems out-of-equilibrium structures may be populated in solution and therefore contribute to the spectral signal. A conformational sampling based on a molecular dynamics allows one to fully sample the phase space. In addition, atomistic methods also directly sample the solvent configurations around the solute, while continuum models assume that the continuum faithfully describe the implicit average over all such considerations. These considerations apply to all atomistic QM/classical approaches. We refer the interested reader to a recent tutorial review[102] for more details, while in the following we focus on the problem of modeling the solute-solvent interaction at the quantum level specifically for the simulation of chiroptical properties, which are often especially sensitive to the solvation environment. Among the different polarizable QM/MM approaches, the QM/Fluctuating Charge

(QM/FQ)[22,102], which is briefly reviewed in the next section, has been especially developed for the purpose of modeling spectroscopic properties of molecules in aqueous solution.[22,102,134–137] QM/FQ has also been amply extended and challenged to treat the most common chiroptical spectroscopies, such as ECD, ORD, VCD and ROA.[57,60,106,138] In this perspective, the performances and the main advantages of using the QM/FQ approach rather than the usual QM/PCM are amply discussed for selected chiral molecules in aqueous solution, for which experimental chiroptical spectra are available.

2 The QM/FQ Approach for Chiroptical Properties

When it is applied to solvated systems, the QM/FQ approach follows the strategy of the so-called "focused models", i.e. it treats the target system at the QM level, whereas the solvent molecules are described at a lower level of theory, and in particular by means of the classical FQ force field. The latter is based on the concepts of atomic hardness and electronegativity, which can be rigorously defined within the so-called "conceptual DFT" framework[139,140]. In particular, the FQ atoms are described in terms of a set of classical point charges, whose value is not fixed, but varies depending on the differences in the electrostatic potential due to the QM density and on the atomic electronegavities. Charge equilibration is obtained according to the electronegativity equalization principle (EEP).[139,141,142]

Based on this theoretical framework, the FQ charges q are obtained through the minimization of the following functional F:

$$F(\mathbf{q},\boldsymbol{\lambda}) = \sum_{\alpha,i} q_{\alpha i}\chi_{\alpha i} + \frac{1}{2}\sum_{\alpha,i}\sum_{\beta,j} q_{\alpha i}J_{\alpha i,\beta j}q_{\beta j} + \sum_{\alpha}\lambda_{\alpha}(\sum_{i} q_{\alpha i} - Q_{\alpha})$$
$$= \mathbf{q}^{\dagger}\boldsymbol{\chi} + \frac{1}{2}\mathbf{q}^{\dagger}\mathbf{J}\mathbf{q} + \boldsymbol{\lambda}^{\dagger}\mathbf{q} \quad (1)$$

where α and β run on molecules and i,j on atoms; λ_{α} is a set of Lagrangian multipliers which are needed to make sure the total charge on molecule α sums to the value Q_{α}. The $\boldsymbol{\chi}$ vector collects atomic electronegativities, and the $\mathbf{J}$ matrix collects the interaction kernel elements between the FQ charges q; the diagonal elements of $\mathbf{J}$ account for charge-charge self-interaction, and are expressed in terms of the chemical hardness η. Non-diagonal terms may be specified through the Ohno functional[143] or alternative formulations.[107,144–146]

The stationarity conditions of the functional in Eq. 1 are defined through the following equation:[107]

$$\mathbf{D}\mathbf{q}_{\boldsymbol{\lambda}} = -\mathbf{C}_{Q} \quad (2)$$

where $\mathbf{C}_{Q}$ collects atomic electronegativities and total charge constraints, whereas charges and Lagrange multipliers are specified in $\mathbf{q}_{\boldsymbol{\lambda}}$. $\mathbf{D}$ collects the $\mathbf{J}$ matrix and the Lagrangian blocks.

When coupled to a QM Hamiltonian, the electrostatic interaction between the FQ charges and the QM density ρ_{QM} reads:[108]

$$E_{\mathrm{QM/MM}} = \sum_{i=1}^{N_q} V[\rho_{QM}](\mathbf{r}_i)q_i \quad (3)$$

where $V[\rho_{QM}](\mathbf{r}_i)$ is the electrostatic potential generated by the QM density at the i-th FQ charge q_i placed at position $\mathbf{r}_i$.

At the Self Consistent Field (SCF) level of theory, the global energy functional of the QM/FQ system then reads:[108]

$$\mathscr{E}[\mathbf{P},\mathbf{q},\boldsymbol{\lambda}] = \mathrm{tr}\mathbf{h}\mathbf{P} + \frac{1}{2}\mathrm{tr}\mathbf{P}\mathbf{G}(\mathbf{P}) + \mathbf{q}^{\dagger}\boldsymbol{\chi} + \frac{1}{2}\mathbf{q}^{\dagger}\mathbf{J}\mathbf{q} + \boldsymbol{\lambda}^{\dagger}\mathbf{q} + \mathbf{q}^{\dagger}\mathbf{V}(\mathbf{P}) \quad (4)$$

where $\mathbf{h}$ and $\mathbf{G}$ are the usual one- and two-electron matrices, and $\mathbf{P}$ is the QM density matrix.

The functional in Eq. 4 can be variationally minimized with respect to FQ charges and lagrangian multipliers. The FQ charges at equilibrium with the external QM potential are obtained by solving the following linear system:[108]

$$\mathbf{D}\mathbf{q}_{\boldsymbol{\lambda}} = -\mathbf{C}_{Q} - \mathbf{V}(\mathbf{P}) \quad (5)$$

A modified Fock $\tilde{\mathbf{F}}$ can therefore be obtained by adding a term which depends on the FQ charges, to standard operators for the isolated system, i.e.:[108]

$$\tilde{F}_{\mu\nu} = \frac{\partial\mathscr{E}}{\partial P_{\mu\nu}} = h_{\mu\nu} + G_{\mu\nu}(\mathbf{P}) + \mathbf{q}^{\dagger}\mathbf{V}_{\mu\nu} \quad (6)$$

where μ, ν indicate atomic basis functions.

2.1 Chiroptical properties/spectroscopies

As stated above, the QM/FQ approach is defined through a variational formulation, i.e. an energy functional is minimized.[108,147] The variational property is quite important in the context of computational spectroscopy because it permits the formal extension of the approach to the evaluation of molecular properties and spectroscopies of any order,[147] by exploiting the machinery of quantum chemistry, which is based on response equations and analytical derivatives. The QM/FQ mutual polarization terms are relatively simple to differentiate analytically to high order, producing terms easily implemented and added to the standard response theory machinery which is used for the calculation of spectroscopic properties of systems in the gas phase. QM/FQ has indeed been implemented and tested for the calculation of a wide variety of properties/spectroscopies, involving purely electric/vibrational/magnetic responses, and their combinations (which give rise to chiroptical signals).[57,60,108,125,148] In the following section we will review how the FQ terms must be included within response equations in order to produce the correct description for the spectroscopic signals of systems in solution.

2.1.1 Optical Rotation and Electronic Circular Dichroism

The simplest chiroptical spectroscopy that can be calculated is arguably electronic circular dichroism (ECD), which requires the evaluation of excited-state energies and transition densities. Once transition densities are obtained, simple absorption and ECD cross sections can be evaluated by computing dipole strengths and rotatory strengths. The standard way to calculate transition properties in DFT is to resort to Time-Dependent Density Functional Theory (TD-DFT)[149], which has been extended to the QM/FQ model through the inclusion of the embedding-dependent terms in the response operators.[108,150]

In particular, TD-DFT equations for a QM/FQ system read:

$$\begin{pmatrix} \tilde{\mathbf{A}} & \tilde{\mathbf{B}} \\ \tilde{\mathbf{B}}^* & \tilde{\mathbf{A}}^* \end{pmatrix} \begin{pmatrix} \mathbf{X} \\ \mathbf{Y} \end{pmatrix} = \omega \begin{pmatrix} \mathbf{1} & \mathbf{0} \\ \mathbf{0} & -\mathbf{1} \end{pmatrix} \begin{pmatrix} \mathbf{X} \\ \mathbf{Y} \end{pmatrix} \tag{7}$$

where $\tilde{A}$ and $\tilde{B}$ matrices are defined as:

$$\tilde{A}_{ai,bj} = (\varepsilon_a - \varepsilon_i)\delta_{ab}\delta_{ij} + (ai|bj) - c_x(ab|ij) + c_l f^{xc}_{ai,bj} + C^{QM/FQ}_{ai,bj} \tag{8}$$

$$\tilde{B}_{ai,bj} = (ai|bj) - c_x(aj|ib) + C^{QM/FQ}_{ai,bj} \tag{9}$$

where $(pq|rs)$ are two electron integrals, ε are molecular orbital (MO) energies, and ω are the excitation energies. c_x and c_l are coefficients, the definition of which depends on the SCF level exploited (c_x =1, c_l = 0 for Hartree-Fock (HF) wavefunctions, c_x =0, c_l = 1 for Density Functional Theory (DFT)).

$C^{QM/FQ}_{ai,bj}$ indicates additional contributions to the $\tilde{A}$ and $\tilde{B}$ matrices due to the presence of the FQ layer. Such terms are defined as:

$$C^{FQ}_{ai,bj} = \sum_p^{N_q} \left(\int_{\mathbb{R}^3} \varphi_a(\mathbf{r}) \frac{1}{|\mathbf{r} - \mathbf{r}_p|} \varphi_i(\mathbf{r})\, \mathrm{d}\mathbf{r} \right) \cdot q_p^T(\varphi_b, \varphi_i) \tag{10}$$

where N_q is the number of the FQ perturbed charges q^T (placed at positions $\mathbf{r}_p$), which are adjusted to the transition density $\mathbf{P}^T_K = \mathbf{X}_K + \mathbf{Y}_K$.[108] φ indicates occupied (i,j indexes) or virtual (a,b indexes) MO orbitals.

The solution of the response equations in 7 yields excitation energies and transition amplitudes; ECD rotatory strength tensors can be computed from such quantities by resorting to the velocity-gauge formalism (see Ref. 79).

From the phenomenological point of view, the simplest chiroptical signal is optical rotation (OR, indicated with ϕ), which can be defined as:[21,78,79,151–155]

$$\phi(\nu) = \frac{16\pi^3 N \nu^2}{c^2} G'(\nu)$$

where

$$G = \frac{1}{3} \mathrm{tr}\, G'_{\alpha\beta}$$

where N is the molecular number density of the system, ν is the frequency of the probing light, and c is the speed of light. $G'_{\alpha\beta}$ is the electric dipole - magnetic dipole polarizability tensor with $\{\alpha,\beta\} = \{x,y,z\}$, i.e.:

$$G'_{\alpha\beta} = \frac{hc}{3\pi} \Im \left\langle \frac{\partial \Psi}{\partial E_\alpha(\nu)} \middle| \frac{\partial \Psi}{\partial B_\beta} \right\rangle \tag{11}$$

where $\Im$ indicates the imaginary part. The integral in Eq. 11 requires the evaluation of the derivatives of the wavefunction Ψ with respect to electric ($\frac{\partial \Psi}{\partial E(\nu)}$) and magnetic ($\frac{\partial \Psi}{\partial B}$) fields. From the computational point of view, such terms can be evaluated by solving the Coupled Perturbed HF/Kohn-Sham (CPHF/KS) equations. For the QM/FQ system, the standard equations for isolated molecules need to be modified so to account for additional terms entering the definition of the response matrices (see Ref. 108 and the section below on ROA for further details).

2.1.2 Vibrational Optical Activity

In order to extend the QM/FQ approach to vibrational optical activity (VOA) we must discuss how the "focused" model approach is applied to separate the vibrational degrees of freedom of the solute from those of the solvent. Properties of the solvated system are thought as originating from the QM portion only, whereas the FQ layer modifies, but not determines them. For this reason, when treating vibrational signals, it is particularly beneficial to resort to the so-called Partial Hessian Vibrational Approach (PHVA),[156–158] where only geometrical perturbations of QM portion are considered, leaving MM atoms frozen.[57,60,125,159]

The most common VOA technique is VCD. As in the case of ECD, intensities are proportional to Rotational Strengths (RS), i.e. the imaginary part of the product between the electric and the magnetic dipole moments. RS can be expressed in terms of two tensors, namely the Atomic Polar Tensor (APT) and the Atomic Axial Tensor (AAT), which are defined as:[3,160–163]

$$\begin{aligned} (\mathrm{APT})^\lambda_{\alpha\beta} &= E^\lambda_{\alpha\beta} + N^\lambda_{\alpha\beta} = \\ &= 2 \left\langle \left(\frac{\partial \Psi_G}{\partial X_{\lambda\alpha}} \right)_{R_0} \middle| (\mu^e_{el})_\beta \middle| \Psi^0_G \right\rangle + Z_\lambda e \delta_{\alpha\beta} \end{aligned} \tag{12}$$

$$\begin{aligned} (\mathrm{AAT})^\lambda_{\alpha\beta} &= I^\lambda_{\alpha\beta} + J^\lambda_{\alpha\beta} = \\ &= \left\langle \left(\frac{\partial \Psi_G}{\partial X_{\lambda\alpha}} \right)_{R^0} \middle| \left(\frac{\partial \Psi_G}{\partial B_\beta} \right)_{B_\beta = 0} \right\rangle + \frac{i}{4hc} \sum \varepsilon_{\alpha\beta\gamma} R^0_{\lambda\gamma} (Z_\lambda e) \end{aligned} \tag{13}$$

where μ^e_{el} is the electronic part of μ_{el} while $Z_\lambda e$ and R^0_λ are the charge and position of nucleus λ at the equilibrium geometry R^0. Ψ_G is the wave function of the ground electronic state, whereas $(\partial \Psi_G / \partial X_{\lambda\alpha})$ and $(\partial \Psi_G / \partial B_\beta)$ are the derivatives of the wavefunction with respect to nuclear displacement and magnetic field, respectively. FQ contributions affect the computed RS. In fact, they modify both the wavefunction and its derivatives. In particular, RSs are calculated by solving the CPHF/CPKS equations (modified so to properly account for gauge-invariance magnetic terms, through the Gauge Including Atomic Orbital–GIAO approach) where FQ contributions are introduced.[148]

We now move to Raman Optical Activity (ROA). By exploiting the Placzek approach within the harmonic approximation,[18] Raman and ROA intensities are obtained in terms of geometrical derivatives of electric dipole-electric dipole polarizability α^x, electric dipole-electric quadrupole polarizability A^x and electric dipole-magnetic dipole polarizability G'^x.[18] In particular, Raman intensities depend on α^x, whereas ROA intensities depend on all three terms, i.e. α^x, A^x and G'^x. In the following equations the QM/FQ contributions to these quantities are reported; more details on the derivation can be found in Ref. 57.

$$\alpha^x_{QM/FQ} = \sum_{\mu\nu}\left[\mathbf{q}^\dagger(\mathbf{P}^e(\omega))\mathbf{V}^x_{\mu\nu}P^e_{\mu\nu}(\omega)\right] + \sum_{\mu\nu}\left[\mathbf{q}^\dagger(\mathbf{P}^e(\omega))\mathbf{V}^x_{\mu\nu}P^e_{\mu\nu}(\omega)\right] \tag{14}$$

$$A^x(\omega)_{QM/FQ} = \sum_{\mu\nu}\left[\mathbf{q}^\dagger(\mathbf{P}^e(\omega))\mathbf{V}^x_{\mu\nu}P^\theta_{\mu\nu}\right] + \sum_{\mu\nu}\left[\mathbf{q}^\dagger(\mathbf{P}^\theta)\mathbf{V}^x_{\mu\nu}P^e_{\mu\nu}(\omega)\right] \tag{15}$$

$$\begin{aligned} G'^x_{QM/FQ} = &\sum_{\mu\nu}\left[\mathbf{q}^\dagger(\mathbf{P}^m)\mathbf{V}^x_{\mu\nu}P^e_{\mu\nu}(\omega)\right] + \sum_{\mu\nu}\left[\mathbf{q}^\dagger(\mathbf{P}^e(\omega))\mathbf{V}^x_{\mu\nu}P^m_{\mu\nu}\right] + \\ &+\sum_{\mu\nu}\left[\mathbf{q}^\dagger(\mathbf{V}^m(\mathbf{P}^e(\omega)))P^x_{\mu\nu}\mathbf{V}_{\mu\nu}\right] + \\ &+\sum_{\mu\nu}\left[\mathbf{q}^\dagger\mathbf{V}^{m,x}_{\mu\nu}P^e_{\mu\nu}(\omega) + \mathbf{q}^{x\dagger}\mathbf{V}^m_{\mu\nu}P^e_{\mu\nu}(\omega)\right] \end{aligned}$$

In the previous equations e, θ and m indicate electric, quadrupole and magnetic perturbations, respectively, whereas ω is the frequency of the external radiation. In Eqs. 14-2.1.2, FQ contributions are expressed in terms of perturbed FQ charges, i.e. generated by a perturbed QM potential. Notice that the additional terms defining G'^x in Eq. 2.1.2, as compared to α^x and A^x are due to the use of GIAOs.[148]

3 Computational Protocol

The calculation of chiroptical signals/spectra with the QM/FQ approach requires one to adhere to the following five-steps protocol.[102,164] This procedure is designed so that computed results are directly comparable with experiments, because they take into account not only the effects of the environment into the calculation of the properties/spectra, but also the fluctuations of the solvent around the solute and their contribution to the final values.[102] As we will show in the next section, such fluctuations (i.e. the actual arrangement of water molecules around the chiral molecule) crucially determine computed values, as well as their sign. It should be kept in mind that some of the following steps involve the selection of parameters which need to be carefully adjusted, because they also substantially determine the quality of the final simulated properties/spectra.

1. *Step 1. Partition of the system*: the "solute" (QM portion), the "solvent" (MM portion) and their boundary need to be defined. The definition may change depending on the system's capability to interact with the environment (especially in case of strong hydrogen bonding interactions taking place between the two layers).

2. *Step 2. Conformational sampling*: the configurational space, i.e. the conformation of the target molecule and the surrounding solvent need to be reliably sampled. This may be done by resorting to (classical) MD, where temperature and pressure are chosen according to experimental data/spectra to be finally modeled. This step also requires one to resort to a parametrized force-field to treat the system classically, which is generally selected according to best practices reported in the literature. Obviously, MD runs need to be long enough to sample the system's entire phase-space in order to obtain spectra that can be considered to be at convergence.

3. *Step 3. Extraction of a set of representative structures:* a number of uncorrelated snapshots are extracted from MD runs and employed for the subsequent QM/MM calculations. In the particular case of QM/FQ we resort to spherical "droplets", which are obtained by cutting spheres of given radii centered on the solute from the generally cubic structures extracted from MD, which are usually run under periodic boundary conditions. The radius of the droplet is chosen to be large enough to retain solute-solvent interactions in a physically consistent way, and is usually of the order of tens of Ångstrom. When in doubt, the convergence of the results with respect to the cutoff radius can be easily assessed on a small number of snapshots. Fortunately, the inclusion of the FQ layer in a quantum chemical calculation does not significantly increase the computational cost, allowing one to extend the size of the droplet to a value considered to be "safe". The total number of snapshots to be extracted cannot be determined "a priori", but it is indeed chosen as the minimum number which yields converged properties/spectra. As we will see in the next section, such a number can vary from hundreds to thousands of snapshots, and it strongly depends on the property/spectroscopy to be computed.[106,159,165]

4. *Step 4. QM/FQ calculations*: a calculation of the target property/spectrum is performed on each of the droplets obtained at the previous step. The QM level of theory is specified according to the state-of-the-art for QM calculations of the same property for isolated systems. In the particular case of vibrational spectra (VCD, ROA) solute structures are minimized in order to find the local minimum of the potential energy surface, by keeping solvent molecules frozen in each droplet. This method preserves the sampling of the water configurational space obtained by means of the MD simulation.[54,60]

5. *Step 5. Analysis of the results and extraction of spectra*: properties and spectra obtained for each droplet are extracted and averaged to produce final results, which are then analyzed and finally compared with experimental data. At this stage, any shortcomings of the procedure may emerge, e.g. an insufficient number of droplets, an insufficiently long MD, a poor choice of classical force field, or inadequacies in the electronic structure method. The procedure may then be restarted from the step(s) that need refinement.

The refinement of the results whose need may emerge during the protocol or at when comparing final results with experiment is especially delicate, and strongly depend on the system at hand and the property one is trying to simulate. Nevertheless, some general considerations may be formulated for Steps 1–4 outlined above:

- Step 1: The partitioning of the system between the QM and MM portions may require a revision. This can be the case if

some of the experimental bands are not predicted by the theoretical model, and such bands are later identified as emerging from parts of the systems outside the focused layer in light of the comparison. In fact, it may be the case that bands can be directly due to solvent vibrational modes (for instance, the chirality transfer bands in the VCD spectrum of ML, *vide infra*), which will require the inclusion of some water molecules in the QM portion to be effectively reproduced.

- Step 2: This step is arguably the most crucial for a correct reproduction of the experimental data. Alas, assessing the quality of the configurational sampling is especially difficult because the latter is not known a priori. Our experience suggests that the correct choice is to exploit force fields that have been amply tests for the specific studied molecular system, therefore an accurate search of the relevant literature for possible pitfalls in the chosen classical parametrization should be done. In the case of smaller systems, a different strategy may be employed: a new parametrization that is specific for the target system may be generated starting from quantum-mechanical calculations,[159,165] which employ an ad-hoc methodology to generate MD parameters from ab-initio calculations.[166] Finally, while a standard MD is more than enough to sample the water configurational space, in the case of very large and flexible solutes it may be necessary to resort to enhanced-sampling techniques in order to explore the full potential energy surfaces, therefore this source of error should be kept in mind for such systems.

- Step 3: This is the easiest step to be controlled, because it is sufficient to increase the number of snapshots extracted from the MD simulation to check the convergence of the computed spectrum. This check should always be performed as an integral part of the protocol: spectra should be plotted against the number of snapshot to verify that convergence has been achieved.

- Step 4: The choice of the QM level, i.e. the combination of Hamiltonian and basis set, is of course paramount and is at the basis of any quantum chemical calculation. As refined as the solvation model may be, it inevitably rests upon the appropriateness of the selected electronic structure model for the specific molecule and property. Any embedding approach can only build upon a model that is assumed to be suitable for the isolated system within a desired accuracy. Therefore, the choice must begin with a search within the relevant literature for appropriate benchmarks to use as a starting point and, if the available data are too general or involve systems that are only distantly related to the ones under investigation or apply to different molecular properties than the one that is being investigated, a new benchmark may be needed, particularly if a failure of the electronic structure model is suspected to be the main source of error.

4 Selected applications

4.1 Optical Rotation

Optical rotation is the oldest of all chiral techniques and the simplicity of its definition and measurement clashes spectacularly with the difficulty encountered in its accurate simulation through ab-initio methods. Even restricting oneself to the description of isolated molecules in the gas phase it has been shown that even qualitatively accurate results may require a complex and often computationally demanding treatment of effects such electron correlation and vibrational anharmonicity.[151,167,168] Experiments measuring the optical rotatory dispersion of molecular systems, however, are almost never performed on gas-phase systems due to the fact that the rotatory power of molecules is so low that it would require an unfeasibly large optical path to produce a signal large enough to be recorded with modern detectors. In fact, only recently have special experimental techniques been developed that allow for the measurement of gas-phase optical rotatory dispersion data,[25] though they still require the system to be volatile and are by no means widely available. Optical rotation, therefore, is invariably bound to the solvated phase, and for computational techniques to assist experimental measurements in any way they must include a treatment of solvation effects.

The presence of the solvent may be naively regarded as a simple perturbation on the system because most common solvents are non-chiral, however it has been shown that even in the case of simple rigid organic molecules varying the solvent can bring huge changes on the measured property.[169]

Continuum solvation models have long been applied to OR calculations,[89] because of their favorable compromise between accuracy and computational cost,[155] and they have shown to be able provide, in some cases, quantitative results.

The applicability of continuum solvent models for different solvents has been explored in Ref. 28, wherein the optical rotation of (*R*)-methyloxirane was simulated for six different solvents of vastly different polarity, from cyclohexane to water. For three of the chosen solvents, i.e. cyclohexane, acetone, and acetonitrile, the method yielded quantitative results, whereas for chloroform, benzene, and water, much greater errors resulted (see Ref. 28 for more details). So great is the error in the case of water that the sign of the property itself is wrong, which is particularly damning because, if used as a predictive tool, the simulation would lead to a wrong assignment of the absolute configuration of the sample.

In the case of water, the harshest simplification imputed to continuum models is the neglect of the directional component of the hydrogen bonding interaction which forms between the water and the oxygen atom of (*R*)-methyloxirane. The FQ method of solvation retains all of the atomistic detail of the solvent and, as discussed in the Theory section, is particularly appropriate for the description of water. In fact, the correct sign and magnitude of the optical rotation of (*R*)-methyloxirane is correctly recovered through a careful application of the method.[106]

QM/MM methods do not just offer a refined description of the solute-solvent interaction, they also allow for a more realistic sampling of the solute's conformational space. Optical rotatory dispersion is exceptionally dependent upon a molecule's confor-

mation, especially when compared to other chiral properties. For instance the sign and intensity of an electronic circular dichroism band can usually be rationalized in terms of the orbital excitations involved in the electronic transition. If the latter is localized on a specific chromophore within the molecule, large side chains spatially separated from the chromophore can be of little influence on the signal. Optical rotation, however, is a global property of the entire molecule. Small fluctuations in the solute's structure or in the disposition of solvent molecules around it may result in large changes in rotatory power. Therefore, a correct description of the solute's conformational distribution, and how it is affected by the surrounding aqueous environment, are crucial.

One example is that of (*R*)-Glycidyl-Methyl-Ether ((*R*)-GME) (see Fig. 1) in water, whose optical rotatory power was investigated in Ref. 165.

To analyze the effect of an atomistic environment to the conformational distribution of (*R*)-GME, standard MD runs have been complemented by MD runs where the position of the non-bonding electron pairs that can act as hydrogen bond acceptors are properly modelled through the definition of virtual sites (VSs) placed near oxygen atoms (see Ref. 165 for more details). In this way, a refined description of the directionality of hydrogen bonding is obtained.

Fig. 1 summarizes the results. For the purpose of comparing results from the two MDs, the conformation of the solute is described in terms of the two dihedral angles from Fig. 1 and for each structure the corresponding OR at the sodium D-line wavelength (589 nm) is represented using a color map. In Fig. 1 we show the OR computed on the snapshots extracted from the MD performed without and with VSs (panel b). The conformational maps generated by the two MDs are completely different as seen from the density of points in the plots.

In particular, the MD employing virtual sites allows for the population of conformational states with θ around 180° while depopulating those around $\theta = 0°$. This has severe consequences towards the calculation of the OR, because different conformations have massively different OR values (notice that the color scale for the OR goes from -400 to $+400$ deg dm^{-1} (g/mL)$^{-1}$).

The resulting OR average values are -32 for the MD without VSs and -7 for the MD with VSs while the experimental value is -17 (all in units of deg dm^{-1} (g/mL)$^{-1}$). In absolute terms a proper account of the directionality of hydrogen bonding achieves a lower error compared to experiment, however it should be clear from the discussion that the large error stems from the high sensitivity of OR to the molecular environment.

From the discussion reported in this section, it should be clear that the QM/FQ method has proven very effective in reproducing the effect of solvation upon the OR of rigid system in aqueous solution, however it still heavily relies on an accurate MD sampling in case of flexible systems. Another consequence of the extremely high range of variation of the OR across the set of extracted snapshot is the necessity for a very large number of them to achieve convergence, much more than any other chiral property ever evaluated with the QM/FQ method of solvation. For (*R*)-GME, for instance, convergence is reached for a total of 8000 snapshots included in the final average, whereas 2000 snapshots are required to reach convergence for the rigid (*R*)-methyloxirane.

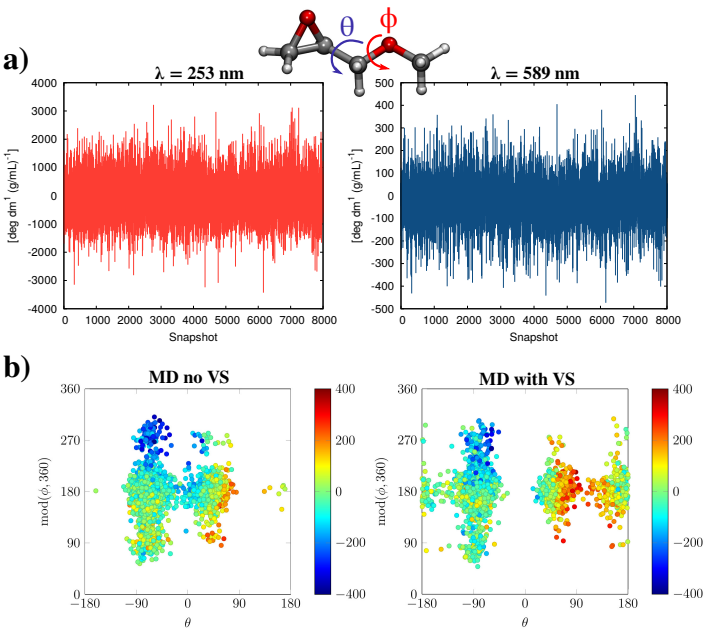

Fig. 1 (a) Calculated QM/FQ OR of aqueous *R*-GME at two different wavelenghts for the various snapshots extracted from MD simulations. (b) Calculated OR at 589 nm for individual configurations obtained from MD simulations of aqueous *R*-GME. Discrete markers are color coded according to the optical-rotation scale in the legend. The two panels illustrate the influence of excluding (left) and including (right) virtual sites on MD simulations. QM level: B3LYP/aug-cc-pVDZ.

4.2 Electronic Circular Dichroism

A cognate property of ORD is ECD. The two properties are related through the Kramers-Kronig relation,[18] and in fact ORD is sometimes estimated experimentally from the ECD spectrum, since this gives the frequency-dependent ORD directly, while a common polarimeter works only at specific wavelengths, though the truncation of the ECD spectrum at higher energies caused by the detection limit of most spectrometers is a source of error. Related as the two properties may be, from the computational point of view their simulation presents different problems and peculiarities.

Similarly to ORD, accurate conformational sampling is needed to obtain a good description of experimental spectra. As an example, we first look at the case of (S)-nicotine in water.[138] In the gas phase nicotine exists mainly in two distinct conformers identified with the letters A and B, with A being the most populated (about 70%, see Fig. 2).[170] In aqueous solution these two structures can also be observed, but they are accompanied by a third conformation which is stabilized thanks to a network of jointly hydrogen-bonded water molecules connecting the two nitrogen atom of the molecule (see Fig. 2a). Note that the PCM does not find this latter conformer, with important consequences on the final spectrum, and substantial inaccuracy in the description of the experimental data.[170] The computed QM/FQ spectrum, shown in Fig. 2c, is in very good agreement with experiment, both with regard to relative intensities and especially sign alternation patterns, the intrinsic limitations of the underlying QM density func-

tional model notwithstanding (which mainly cause a shift of the bands to higher energies).

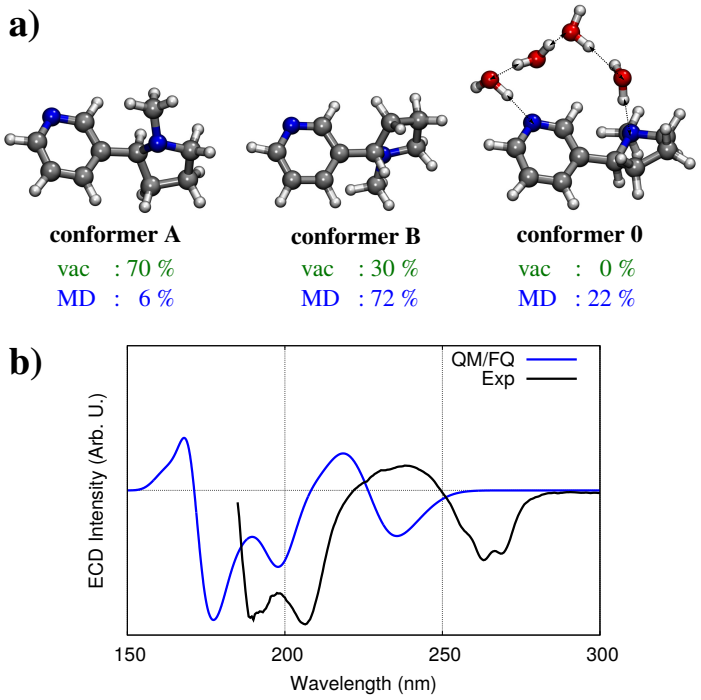

Fig. 2 a) (S)-nicotine conformers with their populations in vacuo (top, green) or from the MD simulation (bottom, blue). (b) Nicotine experimental and calculated QM/FQ ECD spectra (see Ref. 138 for details). QM level: CAM-B3LYP/aug-cc-pVDZ.

As an additional example we look at the ECD spectrum of the anti-inflammatory drug (S)-naproxen (NAP) in water. NAP can freely rotate around two dihedral angles δ_1 and δ_2 (see Fig. 3, panel a). PCM yields four main conformers (see red dots in Fig. 3, panel a), whereas MD samples a much wider region of the conformational space (blue triangles).

The resulting QM/FQ ECD spectrum is reported in Fig. 3 panel b together with the associated raw data, given as a stick spectrum. Clearly, the simple (+,-) pattern hides a great complexity behind the average. In fact, positive and negative signals overlap to produce the averaged band and the final sign pattern. Also, the almost negligible ECD spectral intensity between 275 and 325 nm is the result of a fine balance between sign alternated peaks.

In Fig. 3, panel c, the QM/FQ ECD spectrum is compared to the the experiment, reported in Ref. 171. The computed spectrum is in almost perfect agreement with experiment and, remarkably, all spectral features (peaks sign, band broadening and relative intensities) match between the two spectra.

For the sake of comparison, the QM/PCM ECD spectrum is depicted in the bottom panel of Fig. 3. The continuum approach fails to even qualitatively reproduce the experimental spectrum: the weakly positive band at $\sim$ 260 nm is followed by a strongly positive band at higher energy ($\sim$ 240 nm), rather than the expected negative band. Two strongly negative bands appear at about 210 and 225 nm, thus further decreasing the quality of the reproduction of the experimental findings. As it stands, the computed QM/PCM spectrum would not be accurate enough to provide a correct assignment of the absolute configuration of this molecule, were it unknown.

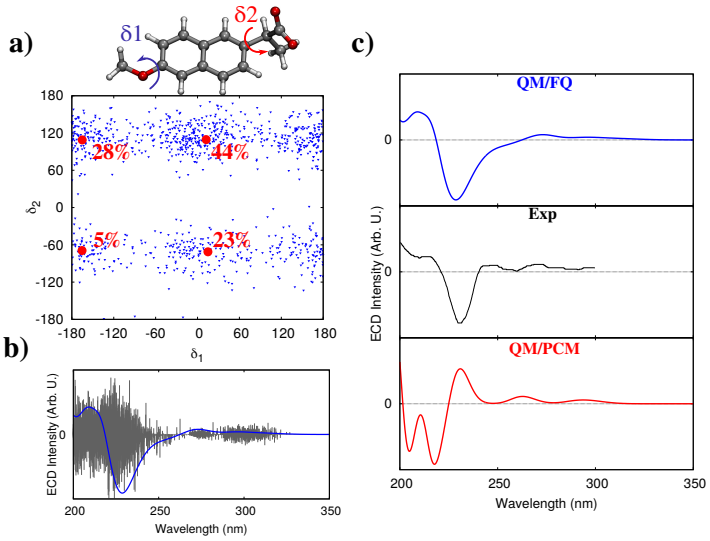

Fig. 3 a) QM/PCM Boltzmann populations (red spots) and MD conformational analysis (blue triangles) for (S)- naproxen in aqueous solution. (b) QM/FQ stick and convoluted ECD spectrum. (c) QM/FQ (top), experimental[171] (middle, and QM/PCM (bottom) ECD spectra of Naproxen in aqueous solution. QM level: CAM-B3LYP/aug-cc-pVDZ.

4.3 Vibrational Circular Dichroism

The VCD spectrum of a molecule was first measured in the 1970s, and is defined as the circular dichroism resulting from vibrational transitions.

Due to the peculiar sensitivity of the VCD signal to the conformational state of molecular systems, it has been widely applied to a large variety of organic and biological molecules. Most VCD experiments are carried out for liquids or solution-state samples, and only few VCD measurements in the gas phase and in the solid phase have been reported. As previously discussed for OR and ECD, also VCD signals can be substantially affected by the external environment, in both sign and magnitude.

As a case study to analyze the effect of the aqueous medium on VCD , we firstly focus on (L)-alanine in the zwitterionic form, for which the most intense region of the spectrum occurs between 1250 and 1450 cm^{-1}; the VCD signal is almost absent in the other regions.[60]

In Figure 4, QM/FQ is employed with the aim of reproducing the experimental spectrum. The top panel shows both the convoluted spectrum and the signals obtained from each snapshot. We clearly notice that the simulated spectrum results from signals whose sign and magnitude vary quite a lot (top panel of Figure 4). As a result of this variability, 1000 snapshots are needed to reach the convergence of the final spectrum, thus suggesting that solvent fluctuations are in this particular case hugely relevant and also difficult to model. In Figure 4, the experimental VCD spectrum measured by Diem[172] is also reported (middle panel). The agreement between QM/FQ spectrum and experiment is evident,

except for the relative intensity the two positive peaks at 1300 cm^{-1} and 1410 cm^{-1}; however, the sign pattern is correctly reproduced.

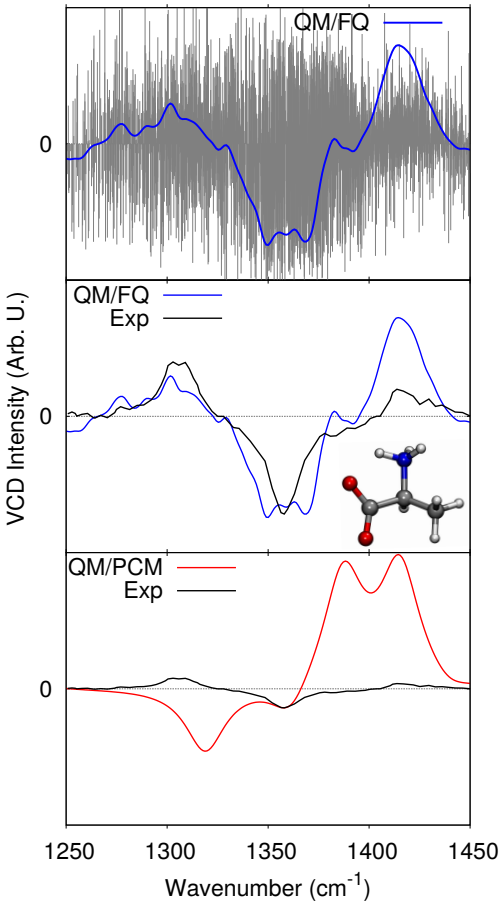

Fig. 4 QM/FQ VCD stick and convoluted spectra (blue, top), experimental [172] (black, middle) and QM/PCM (red, bottom) of (L)-alanine in aqueous solution. QM level: B3LYP/6-311++G**. Note that computed spectra are scaled so that the negative peak at about 1360 cm^{-1} has the same wavenumber and intensity as in the experimental spectrum.

The data reported in Figure 4 also confirm the importance of coupling an atomistic picture of the solvent with a dynamical description of the solvation phenomenon (reproduced through MD). In fact, the static PCM approach, can neither correctly reproduce the sign alternation pattern (see Fig. 4, bottom) nor peaks relative intensities. The normal modes involved in the vibrational transitions in both QM/PCM and QM/FQ spectra are limited to the symmetric stretching of the CO_2^- group and a pair of orthogonal methine CH bending modes, that in agreement with what reported by Nafie.[2] Therefore, the completely different spectral pattern can primary be attributed to the relevance of explicit solvent effects on the molecular geometry, as it is demonstrated by the Root Mean Square Deviation (RMSD) value of 0.4 Å computed on the structures extracted from MD simulations.

L-alanine in the zwitterionic form is a rigid system, and therefore devoid of complications arising from any conformational freedom which may be affected by the solvent. What happens for flexible molecules? To answer this question we focus on the VCD spectrum of (L)-MethylLactate (ML), which is characterized by two main dihedral angles, which lead to three main conformers identified at the QM/PCM level (see Fig. 5 panel a for the definition of the main dihedral angles). The most populated conformer predicted by QM/PCM is characterized by an intramolecular hydrogen bond. This is not surprising, because in PCM such an interaction overcomes solute-solvent forces. The conformational populations obtained through MD simulation is completely different, with the most populated region in MD being the one that is characterized by ML structures where the hydroxyl group points towards solvent molecules.

The different conformational landscape yields a much different VCD spectrum. The QM/FQ convoluted and the corresponding stick spectra are reported in Fig. 5, panel b. For each snapshots, different peak signs and intensities are associated to similar normal modes. This is deeply connected with the particular spatial arrangements of both the QM solute and surrounding solvent. Such a sign alternation applies to most of the transitions reported in the studied region (1000-1800 cm^{-1}).

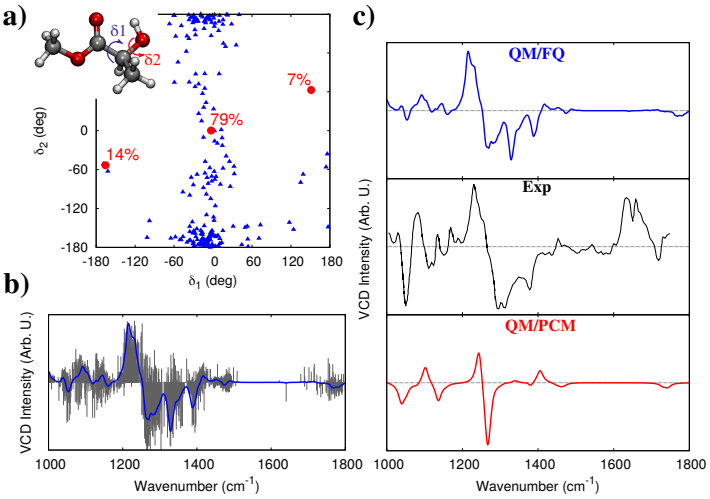

Fig. 5 a QM/PCM Boltzmann populations (red spots) and MD conformational analysis (blue triangles) for (L)-MethylLactate in aqueous solution. b QM/FQ stick and convoluted VCD spectrum and c QM/FQ (top), experimental [112] (middle, neat liquid) and QM/PCM (bottom) VCD spectra QM level: B3LYP/aug-cc-pVDZ.

The average QM/FQ VCD spectrum (Fig. 5, panel c) is characterized by a very distinct pattern (+,-,-,-,+) in the region between 1200 and 1500 cm^{-1}. The large negative peak at about 1280 cm^{-1} and the band at 1380 cm^{-1} are due to two bending modes involving the OH group, which interacts with the solvent via hydrogen bonding interactions. The small negative peak between 1700-1800 cm^{-1} is instead due to the carbonyl stretching.

All the experimental signs and most of the bands' relative intensities in the region between 1200-1500 cm^{-1} are correctly reproduced by QM/FQ (see Fig. 5 panel c). It is also worth remarking that the inhomogeneous band broadening is accurately modelled. This can be evinced by looking at the most intense peak of the spectrum (1220 cm^{-1}), and the negative broad bands between 1300 and 1400 cm^{-1}. The largest discrepancies between QM/FQ and experimental spectra are reported for the VCD signals below 1200 cm^{-1}, for which QM/FQ intensities are generally lower than

their experimental counterparts. Notice however that the vibrational normal modes activated in such a region do not involve any potential site for hydrogen bonding. Therefore, the inaccuracy in the computations may reasonably be related to the chosen level of electronic structure theory or to the huge sign alternation in the bands belonging to this spectral region (see Fig. 5). Nevertheless, the overall band sign is correctly reproduced in this region as well, and so is the band inhomogeneous broadening.

The relevance of specific solvation effects is particularly manifest if QM/FQ is compared to PCM (see Fig. 5, panel c). In fact, the spectral features in the region 1200-1400 cm^{-1} are badly described by PCM: as already discussed, such a range is dominated by vibrational modes directly involving the OH group, which strongly interacts with the surrounding water molecules.[159]

To end the discussion, it is worth pointing out that both QM/PCM and QM/FQ do not reproduce the intense, broad experimental band between 1600 and 1700 cm^{-1}. As previously reported by Xu and co-workers,[111,113,114] such a band is due to the vibrational bending of water molecules, which are chirally activated as a result of the interaction with the chiral solute. Such an effect, which is usually referred to as "chirality transfer", is in this case taking place from ML to the water molecules. It is not surprising that such a band is badly reproduced by both QM/PCM and QM/FQ, which by definition focus only on the spectral signals of the QM solute.

4.4 Raman Optical Activity

ROA is defined as the difference in intensity of the Raman scattered radiation of right and left circularly polarized light. ROA signals can be either positive or negative depending on the absolute configuration of the investigated sample. Similarly to VCD, ROA carries structural information, however it possesses the same advantages that Raman spectroscopy has over Infrared Absorption (IR), such as the possibility of measuring spectra of aqueous systems. Thanks to this peculiarity, the interest on ROA is growing, especially for determining the absolute configuration of biomolecules.

Similarly to the previously discussed chiroptical signals, ROA spectral patterns are strongly dependent upon the molecular environment, therefore ROA simulation benefits from fully atomistic calculations, which also retain polarization effects and the dynamical aspects of the solvation phenomenon.

Let's first focus on the ROA spectrum of ML in aqueous solution, whose VCD spectrum was discussed in the previous section. In Fig. 6 (top panel), the QM/FQ ROA spectrum of ML in water is reported, as obtained by averaging over the same 200 snapshots exploited for the simulation of the VCD spectrum (see previous section). Raw data (stick spectrum) are also superimposed, and clearly show that also for ROA calculated peak intensities result from the average of many signals, which differ both in sign and intensity. Also, a large spread in computed frequencies for each snapshot is noticeable, especially in the regions below 400 cm^{-1} and between 1100 and 1450 cm^{-1}.

In Fig. 6 the computed QM/FQ spectrum is compared to the experimental spectrum taken from Ref.[173] (middle panel). Remarkably, all peak signs are correctly reproduced, as well as relative intensities and band broadening; overall, the accuracy is similar to VCD (see previous section), especially considering that the experimental spectrum is recorded for the neat liquid. The agreement between computed and experimental signals is especially good for the the two small bands at about 1200 cm^{-1}, which are associated to normal modes involving ML OH group. Not surprisingly, the continuum PCM approach (bottom panel in Fig. 6) fails at reproducing the experimental spectrum in this region, due to the lack of any description of hydrogen bonding interactions, which are also present in the neat-liquid.

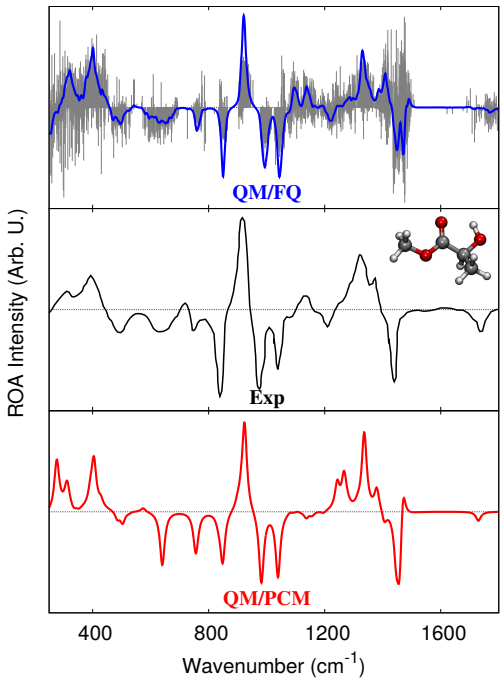

Fig. 6 QM/FQ ROA stick and convoluted spectrum of (L)-MethylLactate in aqueous solution (top), experimental spectrum reproduced from Ref.[173] (neat liquid, middle), and QM/PCM spectrum (bottom). Excitation wavelength: 532 nm. QM level: B3LYP/aug-cc-pVDZ.

We now move to another challenging system, i.e. (S)-glycidol (GLY) in aqueous solution (see Fig. 7, panel a). Despite its simple structure, GLY is a flexible molecule, which can freely rotate around two main dihedral angles (δ_1 and δ_2). The conformational search performed with the continuum PCM yields eight main conformers (see red spots in panel a of Fig. 7). Among the conformers, the most populated (34%) features an intramolecular hydrogen bonding among the hydroxyl H and the epoxyl O (see Fig. 7, panel a). Again, this is not surprising, because in PCM such an interaction overcomes solute-solvent forces. This picture is only partially confirmed by MD conformational analysis (see blue triangles in Fig. 7, panel a). In fact, the eight conformers are also populated along the MD simulation, however the hydroxyl group preferably points towards water molecules, due to the combination of entropic effects and the stabilizing solute-solvent interaction, which overcomes intramolecular hydrogen bonding.

The resulting QM/FQ ROA spectrum is depicted in Figure 7, panel b, where the corresponding stick spectrum is also given.

Similarly to the previous cases, the final spectrum results from the averaging over positive and negative peaks for each normal mode of each representative structure. Again, inhomogeneous band broadening is considered for each band of the convoluted ROA spectrum.

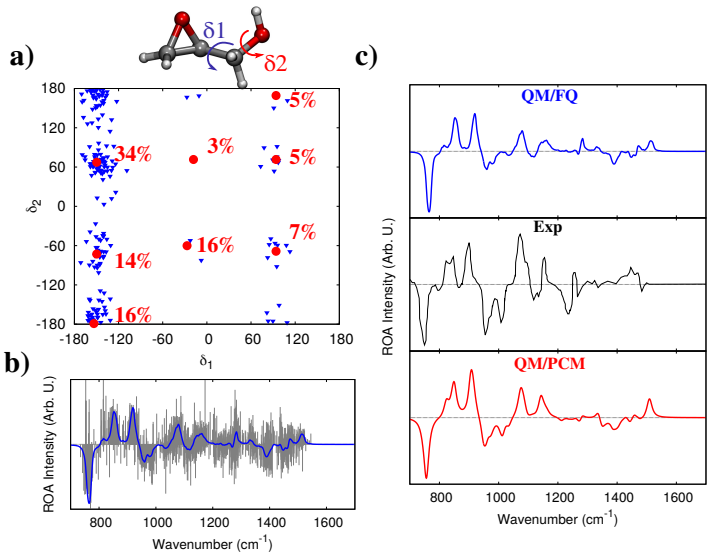

Fig. 7 a QM/PCM Boltzmann populations (red spots) and MD conformational analysis (blue triangles) for (S)-glycidol in aqueous solution. b QM/FQ stick and convoluted ROA spectrum and c QM/FQ (top), experimental[174] (middle, neat liquid) and QM/PCM (bottom) ROA spectra. Excitation wavelength: 514 nm. QM level: B3LYP/aug-cc-pVDZ.

In Fig. 7 QM/FQ is compared to the experimental spectrum measured for the neat liquid.[174] The computed spectrum is characterized by an intense (-,+,+) pattern in the region between 800 and 1000 cm^{-1}, that is associated to normal modes involving the motion of both epoxyl and OH groups. In this region, the computed spectrum is perfectly in agreement with the experiment. The relative intensities of the bands between 950 and 1200 cm^{-1} are not perfectly reproduced, however the inhomogeneous band broadening, and more importantly, the sign alternation pattern, is correctly predicted. The minor differences between QM/FQ and the experimental spectrum may be related to the fact that the latter is measured for the neat liquid, where the extent of intermolecular interactions between GLY-GLY molecules are reasonably different from those modelled by QM/FQ for the aqueous solution.

The limitations of the continuum PCM approach reported in all the previous cases, are less evident for this system. This can be appreciated by inspecting the bottom panel of Fig. 6, panel c. In fact, in this case PCM is able to correctly reproduce the sign pattern.

5 Conclusions

In this perspective we examined the problem of simulating the chiral response of molecules in aqueous solution using multiscale methods for the purpose of both predicting and interpreting chiroptical spectra. The need for accurate predictive tools is especially dire in the context of chiroptical spectroscopies since they can be used to assign the absolute configuration of a sample by comparing the recorded spectrum to its simulated counterpart, though this process requires the underlying methodology to be both reliable and cost-effective. In particular we focused on the treatment of solvation: remarking upon the peculiarities and critical issues of water as a solvent and its effect on the electronic and vibrational properties of systems dissolved within, we argued that common approaches that are often used for other solvents, such as continuum models, are inadequate and can lead to grave errors.

As a solution of this problem we reviewed a multiscale methodology based on the combination of classical MD simulations with a fully polarizable QM/FQ Hamiltonian. Thanks to the classical MD, this methodology allows for a complete sampling of the solute's conformations since it does not rely on the assumption that the solute can be represented by a finite set of rigid minimum-energy structures, and it allows for a completely atomistic description of the solute-solvent configurational space. The subsequent quantum-chemical treatment, based on the QM/FQ approach, is able to fully account for solute-solvent mutual polarization effects in all chiroptical spectroscopies, including OR, ECD, VCD and ROA. The atomistic nature of the approach also allows for an accurate description of Hydrogen Bonding, which is ubiquitous in aqueous solution and can cause drastic changes on the recorded properties, up to sign inversion. Such a feature, together with the accounting of the dynamical aspects of the solvation phenomenon, overcomes the main intrinsic limitations of continuum, static approaches.

The performance of the QM/FQ is are presented and discussed for different molecular systems in aqueous solution, showing an excellent agreement with the experimental measurements. In this way, we clearly demonstrate the reliability of the approach, especially when compared to continuum models. The quality of the results is a consequence of the properties of water: its most important feature, hydrogen bonding, is captured through the atomistic treatment, while the fact that it is a highly polar solvent means that in most cases solvation electrostatics dwarfs other types of interactions. The good agreement with the experimental findings notwithstanding, the approach has additional potentialities that are worth being investigated in the future. Non-electrostatic effects, such as Pauli repulsion and dispersion, could play a non-negligible role.For this reason we have recently developed a model able to account for such interactions in a QM/MM framework,[175,176] and its extension to chiroptical properties can improve the description of aqueous systems but especially pave the way for an accurate simulation of spectral signals of molecules dissolved in non-aqueous solution. In this case, in fact, any limitation to electrostatic-only interactions is not justified.

Also, some features of the experimental VCD spectra presented in this perspective are not reproduced by QM/FQ, due to the fact that it is rooted in the realm of focused approaches. Such bands are due to the so-called "chirality-transfer" effects to eater molecules, which gain rotational strength as a result of the strong interaction with the target system. As stated above, such signals could in principle be predicted by including few, selected water molecules in the QM moiety, however the number and positions

of such solvent molecules are hardly predictable. A promising alternative to such methods is the use of methods rooted in ab-initio MD,[58,177,178], which however have not been amply tested yet in this area.

As we have shown in the previous paragraphs, QM/FQ can accurately reproduce the chiral signals of small-medium molecules dissolved in aqueous solution. However, most of the discussed techniques, and ROA in particular, have been developed to investigate large biological systems, such as proteins or viruses in their natural environment, i.e. the aqueous solution at physiological conditions.[179] The correct and reliable description of such systems has to take into account both the complexity of the biological systems and that given by the interaction with the aqueous environment. A proper theoretical modeling of such agglomerates is still lacking, and it would require enhanced MD sampling techniques, a careful multiscale partitioning of the system, the definition of intermediate layers (especially in case of covalently bound systems) and the correct coupling between all the different interacting parts. Fragmentation techniques are paving the way in this direction.[56,59,180–182] As it stands, though the QM/FQ model in its basic formulation limits the quantum treatment to the solute layer alone with significant computational savings, larger biological systems are out of reach due to the unfavorable scaling of most quantum-based techniques.

Finally, it should be remarked that among chiroptical techniques, the ROA signal is usually quite small in intensity, being the result of a differential third order process. Through state-of-the art ab-initio simulations, we have shown that Resonance ROA (RROA)[183–189] can overcome this limitation because the resonance condition for the probing wavelength can result in an enhancement factor of 10^{2-3}.[190,191] Conversely, from the experimental point of view, measurements of RROA of biological systems can also be measured in the UV range thanks to the recent developments by Kapitan and co-workers.[192] Extension of our QM/FQ to RROA would contribute to the further development of this technique. Another fascinating field, which would deserve the coupling with reliable computational methods is the study of the transfer of chirality mediated by plasmonic nanomaterials, which has been experimentally evidenced.[193] The application of a suitably modified QM/FQ approach to such phenomena, through its extension to treat the specificities of plasmonic materials,[194–196] is under development in our group.

Conflicts of interest

There are no conflicts to declare.

Acknowledgements

TG acknowledges funding from the Research Council of Norway through its grant TheoLight (grant no. 275506).

Notes and references

1 L. A. Nafie, T. Keiderling and P. Stephens, *J. Am. Chem. Soc.*, 1976, **98**, 2715–2723.

2 L. A. Nafie, *Vibrational optical activity: principles and applications*, John Wiley & Sons, Chichester, 2011.

3 P. J. Stephens, F. J. Devlin and J. R. Cheeseman, *VCD spectroscopy for organic chemists*, CRC Press, 2012.

4 N. Berova, L. Di Bari and G. Pescitelli, *Chem. Soc. Rev.*, 2007, **36**, 914–931.

5 P. L. Polavarapu, *Chem. Rec.*, 2007, **7**, 125–136.

6 N. Berova, K. Nakanishi and R. W. Woody, *Circular dichroism: principles and applications*, John Wiley & Sons, 2000.

7 N. Berova, P. L. Polavarapu, K. Nakanishi and R. W. Woody, *Comprehensive chiroptical spectroscopy: applications in stereochemical analysis of synthetic compounds, natural products, and biomolecules*, John Wiley & Sons, 2012, vol. 2.

8 T. B. Freedman, X. Cao, R. K. Dukor and L. A. Nafie, *Chirality*, 2003, **15**, 743–758.

9 R. K. Dukor and T. A. Keiderling, *Biopolymers: Original Research on Biomolecules*, 1991, **31**, 1747–1761.

10 Y. He, W. Bo, R. K. Dukor and L. A. Nafie, *Appl. Spectrosc.*, 2011, **65**, 699–723.

11 P. L. Polavarapu, A. Petrovic and F. Wang, *Chirality*, 2003, **15**, S143–S149.

12 K. Monde, T. Taniguchi, N. Miura, C. S. Vairappan and M. Suzuki, *Tetrahedron Lett.*, 2006, **47**, 4389–4392.

13 X. Li, K. H. Hopmann, J. Hudecova, J. Isaksson, J. Novotna, W. Stensen, V. Andrushchenko, M. Urbanova, J.-S. Svendsen, P. Bouř and K. Ruud, *J. Phys. Chem. A*, 2013, **117**, 1721–1736.

14 J. M. Batista Jr, A. N. Batista, D. Rinaldo, W. Vilegas, Q. B. Cass, V. S. Bolzani, M. J. Kato, S. N. López, M. Furlan and L. A. Nafie, *Tetrahedron-Asymmetr.*, 2010, **21**, 2402–2407.

15 L. G. Felippe, J. M. Batista Jr, D. C. Baldoqui, I. R. Nascimento, M. J. Kato, Y. He, L. A. Nafie and M. Furlan, *Org. Biomol. Chem.*, 2012, **10**, 4208–4214.

16 S. Abbate, L. F. Burgi, E. Castiglioni, F. Lebon, G. Longhi, E. Toscano and S. Caccamese, *Chirality*, 2009, **21**, 436–441.

17 C. Merten, T. P. Golub and N. M. Kreienborg, *J. Org. Chem.*, 2019, **84**, 8797–8814.

18 L. D. Barron, *Molecular light scattering and optical activity*, Cambridge University Press, 2004.

19 T. Helgaker, S. Coriani, P. Jørgensen, K. Kristensen, J. Olsen and K. Ruud, *Chem. Rev.*, 2012, **112**, 543–631.

20 P. Norman, K. Ruud and T. Saue, *Principles and practices of molecular properties: Theory, modeling, and simulations*, John Wiley & Sons, 2018.

21 T. D. Crawford, M. C. Tam and M. L. Abrams, *J. Phys. Chem. A*, 2007, **111**, 12057–12068.

22 C. Cappelli, *Int. J. Quantum Chem.*, 2016, **116**, 1532–1542.

23 P. Stephens and F. Devlin, *Chirality*, 2000, **12**, 172–179.

24 M. Krupová, J. Kessler and P. Bour, *ChemPlusChem*, 2020, **85**, 561–575.

25 T. Müller, K. B. Wiberg and P. H. Vaccaro, *J. Phys. Chem. A*, 2000, **104**, 5959–5968.

26 M. Hodecker, M. Biczysko, A. Dreuw and V. Barone, *J. Chem. Theory Comput.*, 2016, **12**, 2820–2833.

27 T. B. Pedersen, J. Kongsted, T. D. Crawford and K. Ruud, *J. Chem. Phys.*, 2009, **130**, 034310.

28 F. Egidi, V. Barone, J. Bloino and C. Cappelli, *J. Chem. Theory Comput.*, 2012, **8**, 585–597.

29 K. Ruud and R. Zanasi, *Angew. Chem. Int. Ed.*, 2005, **117**, 3660–3662.

30 Y. Liu, J. Cerezo, G. Mazzeo, N. Lin, X. Zhao, G. Longhi, S. Abbate and F. Santoro, *J. Chem. Theory Comput.*, 2016, **12**, 2799–2819.

31 N. Lin, Y. Luo, F. Santoro, X. Zhao and A. Rizzo, *Chem. Phys. Lett*, 2008, **464**, 144–149.

32 J. Cerezo, G. Mazzeo, G. Longhi, S. Abbate and F. Santoro, *J. Phys. Chem. Lett.*, 2016, **7**, 4891–4897.

33 J. Cerezo, D. Aranda, F. J. Avila Ferrer, G. Prampolini, G. Mazzeo, G. Longhi, S. Abbate and F. Santoro, *Chirality*, 2018, **30**, 730–743.

34 L. Barron, L. Hecht, E. Blanch and A. Bell, *Prog. Biophys. Mol. Bio.*, 2000, **73**, 1–49.

35 T. A. Keiderling, *Molecules*, 2018, **23**, 2404.

36 D. Kurouski, R. A. Lombardi, R. K. Dukor, I. K. Lednev and L. A. Nafie, *Chem. Comm.*, 2010, **46**, 7154–7156.

37 P. J. Stephens, *J. Phys. Chem*, 1985, **89**, 748–752.

38 P. J. Stephens, F. J. Devlin and J.-J. Pan, *Chirality*, 2008, **20**, 643–663.

39 K. Ruud and A. J. Thorvaldsen, *Chirality*, 2009, **21**, E54–E67.

40 V. Liégeois, K. Ruud and B. Champagne, *J. Chem. Phys.*, 2007, **127**, 204105.

41 L. Barron and L. Hecht, *Circular Dichroism Principles and Applications*, 2000, 667–701.

42 W. Hug, *Raman optical activity spectroscopy*, Wiley Online Library, 2002.

43 L. D. Barron, F. Zhu and L. Hecht, *Vib. Spectrosc.*, 2006, **42**, 15–24.

44 T. A. Keiderling and A. Lakhani, *Chirality*, 2018, **30**, 238–253.

45 L. A. Nafie, *Chirality*, 2020, **32**, 667–692.

46 L. A. Nafie, in *Frontiers and Advances in Molecular Spectroscopy*, Elsevier, 2018, pp. 421–469.

47 H. Sato, *Phys. Chem. Chem. Phys.*, 2020, **22**, 7671–7679.

48 T. Taniguchi and K. Monde, *J. Am. Chem. Soc.*, 2012, **134**, 3695–3698.

49 T. Fujisawa and M. Unno, *Molecular and Laser Spectroscopy: Advances and Applications: Volume 2*, 2020, 41.

50 G. Longhi, S. Abbate, R. Gangemi, E. Giorgio and C. Rosini, *J. Phys. Chem. A*, 2006, **110**, 4958–4968.

51 P. L. Polavarapu and E. Santoro, *Nat. Prod. Rep.*, 2020, DOI: 10.1039/D0NP00025F.

52 L. A. Nafie, *Annu. Rev. Phys. Chem.*, 1997, **48**, 357–386.

53 P. Polavarapu, *J. Phys. Chem.*, 1990, **94**, 8106–8112.

54 J. R. Cheeseman, M. S. Shaik, P. L. Popelier and E. W. Blanch, *J. Am. Chem. Soc.*, 2011, **133**, 4991–4997.

55 F. Zielinski, S. T. Mutter, C. Johannessen, E. W. Blanch and P. L. Popelier, *Phys. Chem. Chem. Phys.*, 2015, **17**, 21799–21809.

56 K. J. Jose and K. Raghavachari, *J. Chem. Theory Comput.*, 2016, **12**, 585–594.

57 T. Giovannini, M. Olszòwka, F. Egidi, J. R. Cheeseman, G. Scalmani and C. Cappelli, *J. Chem. Theory Comput.*, 2017, **13**, 4421–4435.

58 A. Scherrer, R. Vuilleumier and D. Sebastiani, *J. Chem. Theory Comput.*, 2013, **9**, 5305–5312.

59 K. J. Jose, D. Beckett and K. Raghavachari, *J. Chem. Theory Comput.*, 2015, **11**, 4238–4247.

60 T. Giovannini, M. Olszowka and C. Cappelli, *J. Chem. Theory Comput.*, 2016, **12**, 5483–5492.

61 C. Cappelli, S. Corni, B. Mennucci, R. Cammi and J. Tomasi, *J. Phys. Chem A*, 2002, **106**, 12331–12339.

62 J. Cheeseman, M. Frisch, F. Devlin and P. Stephens, *Chem. Phys. Lett.*, 1996, **252**, 211–220.

63 J. R. Cheeseman, M. J. Frisch, F. J. Devlin and P. J. Stephens, *J. Phys. Chem A*, 2000, **104**, 1039–1046.

64 J. Kongsted, T. B. Pedersen, M. Strange, A. Osted, A. E. Hansen, K. V. Mikkelsen, F. Pawlowski, P. Jørgensen and C. Hättig, *Chem. Phys. Lett.*, 2005, **401**, 385–392.

65 B. Mennucci, C. Cappelli, R. Cammi and J. Tomasi, *Chirality*, 2011, **23**, 717–729.

66 M. Krykunov and J. Autschbach, *J. Chem. Phys.*, 2015, **123**, 114103.

67 K. Ruud and T. Helgaker, *Chem. Phys. Lett.*, 2002, **352**, 533âĂŞ539.

68 S. Luber, C. Herrmann and M. Reiher, *J. Phys. Chem. B*, 2008, **112**, 2218–2232.

69 S. Luber, *J. Chem. Theory Comput.*, 2017, **13**, 1254–1262.

70 M. A. Koenis, L. Visscher, W. J. Buma and V. P. Nicu, *J. Phys. Chem. B*, 2020, **124**, 1665–1677.

71 P. Bouř, K. Záruba, M. Urbanová, V. Setnička, P. Matějka, Z. Fiedler, V. Král and K. Volka, *Chirality*, 2000, **12**, 191–198.

72 J. Hudecova, V. Profant, P. Novotna, V. Baumruk, M. Urbanova and P. Bouř, *J. Chem. Theory Comput.*, 2013, **9**, 3096–3108.

73 C. Johannessen, E. W. Blanch, C. Villani, S. Abbate, G. Longhi, N. R. Agarwal, M. Tommasini and D. A. Lightner, *J. Phys. Chem. B*, 2013, **117**, 2221–2230.

74 S. Abbate, F. Lebon, G. Longhi, F. Fontana, T. Caronna and D. A. Lightner, *Phys. Chem. Chem. Phys.*, 2009, **11**, 9039–9043.

75 C. Merten, *Phys. Chem. Chem. Phys.*, 2017, **19**, 18803–18812.

76 C. Merten and Y. Xu, *ChemPhysChem*, 2013, **14**, 213–219.

77 K. B. Wiberg, M. Caricato, Y.-G. Wang and P. H. Vaccaro, *Chirality*, 2013, **25**, 606–616.

78 P. L. Polavarapu, *Chirality*, 2002, **14**, 768–781.

79 T. B. Pedersen, H. Koch, L. Boman and A. M. S. de Merás, *Chem. Phys. Lett.*, 2004, **393**, 319–326.

80 S. Haghdani, P.-O. Åstrand and H. Koch, *J. Chem. Theory Comput.*, 2016, **12**, 535–548.

81 J. Autschbach, T. Ziegler, S. J. van Gisbergen and E. J.

Baerends, *J. Chem. Phys.*, 2002, **116**, 6930–6940.
82 L. Goerigk and S. Grimme, *J. Phys. Chem. A*, 2009, **113**, 767–776.
83 M. Srebro, N. Govind, W. A. De Jong and J. Autschbach, *J. Phys. Chem. A*, 2011, **115**, 10930–10949.
84 M. Pecul and K. Ruud, *Adv. Quantum Chem.*, 2005, **50**, 185–212.
85 M. Srebro-Hooper and J. Autschbach, *Annu. Rev. Phys. Chem.*, 2017, **68**, 399–420.
86 T. A. Keiderling, *Chem. Rev.*, 2020, **120**, 3381–3419.
87 J. M. Batista Jr, E. W. Blanch and V. da Silva Bolzani, *Nat. Prod. Rep.*, 2015, **32**, 1280–1302.
88 P. Lahiri, K. B. Wiberg, P. H. Vaccaro, M. Caricato and T. D. Crawford, *Angew. Chem.*, 2014, **126**, 1410–1413.
89 T. Aharon, P. Lemler, P. H. Vaccaro and M. Caricato, *Chirality*, 2017, **30**, 383–395.
90 S. M. Wilson, K. B. Wiberg, M. J. Murphy and P. H. Vaccaro, *Chirality*, 2008, **20**, 357–369.
91 E. W. Blanch, L. Hecht and L. D. Barron, *Methods*, 2003, **29**, 196–209.
92 T. Vermeyen and C. Merten, *Phys. Chem. Chem. Phys.*, 2020, **22**, 15640–15648.
93 C. R. Jacob, S. Luber and M. Reiher, *Chem. Eur. J.*, 2009, **15**, 13491–13508.
94 T. Fujisawa, R. L. Leverenz, M. Nagamine, C. A. Kerfeld and M. Unno, *J. Am. Chem. Soc.*, 2017, **139**, 10456–10460.
95 T. Taniguchi, D. Manai, M. Shibata, Y. Itabashi and K. Monde, *J. Am. Chem. Soc.*, 2015, **137**, 12191–12194.
96 M. Unno, T. Kikukawa, M. Kumauchi and N. Kamo, *J. Phys. Chem. B*, 2013, **117**, 1321–1325.
97 J. Kapitán, V. Baumruk and P. Bouř, *J. Am. Chem. Soc.*, 2006, **128**, 2438–2443.
98 J. Hanzlíková, P. Praus and V. Baumruk, *J. Mol. Struc.*, 1999, **480**, 431–435.
99 A. N. Batista, J. M. Batista Jr, V. S. Bolzani, M. Furlan and E. W. Blanch, *Phys. Chem. Chem. Phys.*, 2013, **15**, 20147–20152.
100 A. N. Batista, J. M. Batista Jr, L. Ashton, V. S. Bolzani, M. Furlan and E. W. Blanch, *Chirality*, 2014, **26**, 497–501.
101 F. Eker, X. Cao, L. Nafie and R. Schweitzer-Stenner, *J. Am. Chem. Soc.*, 2002, **124**, 14330–14341.
102 T. Giovannini, F. Egidi and C. Cappelli, *Chem. Soc. Rev.*, 2020, DOI: 10.1039/c9cs00464e.
103 F. Paesani, *Acc. Chem. Res.*, 2016, **49**, 1844–1851.
104 S. Naserifar and W. A. Goddard 3rd, *Proc. Natl. Acad. Sci. USA*, 2019, **116**, 1998–2003.
105 O. Demerdash, L.-P. Wang and T. Head-Gordon, *WIRES Comput. Mol. Sci.*, 2018, **8**, e1355.
106 F. Lipparini, F. Egidi, C. Cappelli and V. Barone, *J. Chem. Theory Comput.*, 2013, **9**, 1880–1884.
107 F. Lipparini and V. Barone, *J. Chem. Theory Comput.*, 2011, **7**, 3711–3724.
108 F. Lipparini, C. Cappelli and V. Barone, *J. Chem. Theory Comput.*, 2012, **8**, 4153–4165.
109 J. Tomasi, B. Mennucci and R. Cammi, *Chem. Rev.*, 2005, **105**, 2999–3094.
110 P. Mukhopadhyay, G. Zuber, M.-R. Goldsmith, P. Wipf and D. N. Beratan, *Chem. Phys. Chem*, 2006, **7**, 2483–2486.
111 M. Losada, P. Nguyen and Y. Xu, *J. Phys. Chem A*, 2008, **112**, 5621–5627.
112 M. Losada and Y. Xu, *Phys. Chem. Chem. Phys.*, 2007, **9**, 3127–3135.
113 G. Yang and Y. Xu, *J. Chem. Phys.*, 2009, **130**, 164506–164506.
114 M. Losada, H. Tran and Y. Xu, *J. Chem. Phys.*, 2008, **128**, 014508.
115 C. Merten and Y. Xu, *Angew. Chem. Int. Ed.*, 2013, **125**, 2127–2130.
116 P. Mukhopadhyay, G. Zuber, P. Wipf and D. N. Beratan, *Angew. Chem. Int. Ed.*, 2007, **46**, 6450–6452.
117 B. Mennucci, *WIREs Comput. Mol. Sci.*, 2012, **2**, 386–404.
118 T. Giovannini, L. Grazioli, M. Ambrosetti and C. Cappelli, *J. Chem. Theory Comput.*, 2019, **15**, 5495–5507.
119 T. Giovannini, R. R. Riso, M. Ambrosetti, A. Puglisi and C. Cappelli, *J. Chem. Phys.*, 2019, **151**, 174104.
120 C. Cappelli, B. Mennucci and S. Monti, *J. Phys. Chem. A*, 2005, **109**, 1933–1943.
121 H. M. Senn and W. Thiel, *Angew. Chem. Int. Ed.*, 2009, **48**, 1198–1229.
122 H. Lin and D. G. Truhlar, *Theor. Chem. Acc.*, 2007, **117**, 185–199.
123 U. N. Morzan, D. J. Alonso de Armino, N. O. Foglia, F. Ramirez, M. C. Gonzalez Lebrero, D. A. Scherlis and D. A. Estrin, *Chem. Rev.*, 2018, **118**, 4071–4113.
124 T. Giovannini, A. Puglisi, M. Ambrosetti and C. Cappelli, *J. Chem. Theory Comput.*, 2019, **15**, 2233–2245.
125 F. Lipparini, C. Cappelli, G. Scalmani, N. De Mitri and V. Barone, *J. Chem. Theory Comput.*, 2012, **8**, 4270–4278.
126 C. Curutchet, A. Muñoz-Losa, S. Monti, J. Kongsted, G. D. Scholes and B. Mennucci, *J. Chem. Theory Comput.*, 2009, **5**, 1838–1848.
127 F. Lipparini, *J. Chem. Theory Comput.*, 2019, **15**, 4312–4317.
128 A. H. Steindal, K. Ruud, L. Frediani, K. Aidas and J. Kongsted, *J. Phys. Chem. B*, 2011, **115**, 3027–3037.
129 T. Schwabe, J. M. H. Olsen, K. Sneskov, J. Kongsted and O. Christiansen, *J. Chem. Theory Comput.*, 2011, **7**, 2209–2217.
130 J. M. H. Olsen and J. Kongsted, *Adv. Quantum Chem.*, 2011, **61**, 107–143.
131 D. Loco, É. Polack, S. Caprasecca, L. Lagardere, F. Lipparini, J.-P. Piquemal and B. Mennucci, *J. Chem. Theory Comput.*, 2016, **12**, 3654–3661.
132 D. Loco, S. Jurinovich, L. Cupellini, M. F. Menger and B. Mennucci, *Photochem. Photobiol. Sci.*, 2018, **17**, 552–560.
133 M. Bondanza, M. Nottoli, L. Cupellini, F. Lipparini and B. Mennucci, *Phys. Chem. Chem. Phys.*, 2020, **22**, 14433–14448.

134 F. Egidi, I. Carnimeo and C. Cappelli, *Opt. Mater. Express*, 2015, **5**, 196–209.

135 F. Egidi, G. Lo Gerfo, M. Macchiagodena and C. Cappelli, *Theor. Chem. Acc.*, 2018, **137**, 82.

136 T. Giovannini, M. Ambrosetti and C. Cappelli, *J. Phys. Chem. Lett.*, 2019, **10**, 5823–5829.

137 S. Gómez, T. Giovannini and C. Cappelli, *Phys. Chem. Chem. Phys.*, 2020, **22**, 5929–5941.

138 F. Egidi, R. Russo, I. Carnimeo, A. D'Urso, G. Mancini and C. Cappelli, *J. Phys. Chem. A*, 2015, **119**, 5396–5404.

139 W. J. Mortier, K. Van Genechten and J. Gasteiger, *J. Am. Chem. Soc.*, 1985, **107**, 829–835.

140 R. Chelli and P. Procacci, *J. Chem. Phys.*, 2002, **117**, 9175–9189.

141 A. K. Rappe and W. A. Goddard III, *J. Phys. Chem*, 1991, **95**, 3358–3363.

142 R. Sanderson, *Science*, 1951, **114**, 670–672.

143 K. Ohno, *Theor. Chim. Acta*, 1964, **2**, 219–227.

144 S. W. Rick, S. J. Stuart and B. J. Berne, *J. Chem. Phys.*, 1994, **101**, 6141–6156.

145 S. W. Rick, S. J. Stuart, J. S. Bader and B. Berne, *J. Mol. Liq.*, 1995, **65**, 31–40.

146 S. W. Rick and B. J. Berne, *J. Am. Chem. Soc.*, 1996, **118**, 672–679.

147 R. Di Remigio, T. Giovannini, M. Ambrosetti, C. Cappelli and L. Frediani, *J. Chem. Theory Comput.*, 2019, **15**, 4056–4068.

148 F. Lipparini, C. Cappelli and V. Barone, *J. Chem. Phys.*, 2013, **138**, 234108.

149 M. E. Casida, in *Recent Advances in Density Functional Methods Part I*, ed. D. P. Chong, World Scientific, Singapore, 1995, pp. 155–192.

150 I. Carnimeo, C. Cappelli and V. Barone, *J. Comput. Chem.*, 2015, **36**, 2271–2290.

151 K. Ruud and T. Helgaker, *Chem. Phys. Lett.*, 2002, **352**, 533–539.

152 A. Buckingham, C. Graham and R. Raab, *Chem. Phys. Lett.*, 1971, **8**, 622–624.

153 P. Stephens, F. Devlin, J. Cheeseman and M. Frisch, *J. Phys. Chem. A*, 2001, **105**, 5356–5371.

154 P. Stephens, F. Devlin, J. Cheeseman, M. Frisch and C. Rosini, *Org. Lett.*, 2002, **4**, 4595–4598.

155 B. Mennucci, J. Tomasi, R. Cammi, J. Cheeseman, M. Frisch, F. Devlin, S. Gabriel and P. Stephens, *J. Phys. Chem. A*, 2002, **106**, 6102–6113.

156 S. Jin and J. D. Head, *Surf. Science*, 1994, **318**, 204–216.

157 M. D. Calvin, J. D. Head and S. Jin, *Surf. science*, 1996, **345**, 161–172.

158 A. Biancardi, R. Cammi, C. Cappelli, B. Mennucci and J. Tomasi, *Theor. Chem. Acc.*, 2012, **131**, 1–10.

159 T. Giovannini, G. Del Frate, P. Lafiosca and C. Cappelli, *Phys. Chem. Chem. Phys.*, 2018, **20**, 9181–9197.

160 R. Amos, N. Handy, K. Jalkanen and P. Stephens, *Chem. Phys. Lett.*, 1987, **133**, 21–26.

161 J. Cheeseman, M. Frisch, F. Devlin and P. Stephens, *Chem. Phys. Lett.*, 1996, **252**, 211–220.

162 P. Stephens and F. Devlin, *Chirality*, 2000, **12**, 172–179.

163 P. J. Stephens, F. J. Devlin and J.-J. Pan, *Chirality*, 2008, **20**, 643–663.

164 T. Giovannini, M. Macchiagodena, M. Ambrosetti, A. Puglisi, P. Lafiosca, G. Lo Gerfo, F. Egidi and C. Cappelli, *Int. J. Quantum Chem.*, 2019, **119**, e25684.

165 F. Egidi, T. Giovannini, G. Del Frate, P. M. Lemler, P. H. Vaccaro and C. Cappelli, *Phys. Chem. Chem. Phys.*, 2019, **21**, 3644–3655.

166 I. Cacelli and G. Prampolini, *J. Chem. Theory Comput.*, 2007, **3**, 1803–1817.

167 C. Cappelli, J. Bloino, F. Lipparini and V. Barone, *J. Phys. Chem.. Lett.*, 2012, **3**, 1766–1773.

168 P. Daněček, J. Kapitan, V. Baumruk, L. Bednárová, V. Kopecký Jr and P. Bouř, *J. Chem. Phys.*, 2007, **126**, 224513.

169 Y. Kumata, J. Furukawa and T. Fueno, *Bull. Chem. Soc. Jpn.*, 1970, **43**, 3920–3921.

170 F. Egidi, M. Segado, H. Koch, C. Cappelli and V. Barone, *J. Chem. Phys.*, 2014, **141**, 224114.

171 V. F. Ximenes, N. H. Morgon and A. R. de Souza, *Chirality*, 2018, **30**, 1049–1053.

172 M. Diem, *J. Am. Chem. Soc.*, 1988, **110**, 6967–6970.

173 S. Qiu, G. Li, P. Wang, G. Jia, Z. Feng and C. Li, *J. Raman Spectrosc.*, 2012, **43**, 503–513.

174 K. M. Spencer, R. B. Edmonds and R. D. Rauh, *Appl. Spectrosc.*, 1996, **50**, 681–685.

175 T. Giovannini, P. Lafiosca and C. Cappelli, *J. Chem. Theory Comput.*, 2017, **13**, 4854–4870.

176 T. Giovannini, P. Lafiosca, B. Chandramouli, V. Barone and C. Cappelli, *J. Chem. Phys.*, 2019, **150**, 124102.

177 A. Scherrer, R. Vuilleumier and D. Sebastiani, *J. Chem. Phys.*, 2016, **145**, 084101.

178 A. Scherrer, F. Agostini, D. Sebastiani, E. Gross and R. Vuilleumier, *J. Chem. Phys.*, 2015, **143**, 074106.

179 L. Barron, E. Blanch and L. Hecht, *Adv. Protein Chem.*, 2002, **62**, 51–90.

180 J. Hudecová and P. Bouř, in *Vibrational Spectroscopy in Protein Research*, Elsevier, 2020, pp. 219–248.

181 J. Kessler, V. Andrushchenko, J. Kapitán and P. Bouř, *Phys. Chem. Chem. Phys.*, 2018, **20**, 4926–4935.

182 S. Luber, J. Neugebauer and M. Reiher, *J. Chem. Phys.*, 2010, **132**, 044113.

183 L. A. Nafie, *Chem. Phys.*, 1996, **205**, 309–322.

184 M. Vargek, T. B. Freedman, E. Lee and L. A. Nafie, *Chem. Phys. Lett.*, 1998, **287**, 359–364.

185 C. Johannessen, P. C. White and S. Abdali, *J. Phys. Chem. A*, 2007, **111**, 7771–7776.

186 S. Yamamoto and P. Bouř, *Angew. Chem. Int. Ed.*, 2012, **51**, 11058–11061.

187 E. Machalska, G. Zajac, A. Gruca, F. Zobi, M. Baranska and A. J. Kaczor, *J. Phys. Chem. Lett.*, 2020, **11**, 5037–5043.

188 G. Li, J. Kessler, J. Cheramy, T. Wu, M. R. Poopari, P. Bouř and Y. Xu, *Angew. Chem. Int. Ed.*, 2019, **58**, 16495–16498.

189 C. Merten, H. Li and L. A. Nafie, *J. Phys. Chem. A*, 2012, **116**, 7329–7336.

190 L. N. Vidal, F. Egidi, V. Barone and C. Cappelli, *J. Chem. Phys.*, 2015, **142**, 174101.

191 L. N. Vidal, T. Giovannini and C. Cappelli, *J. Phys. Chem. Lett.*, 2016, **7**, 3585–3590.

192 J. Kapitán, L. D. Barron and L. Hecht, *J. Raman Spectr.*, 2015, **46**, 392–399.

193 S. Ostovar pour, L. Rocks, K. Faulds, D. Graham, V. Parchaňskỳ, P. Bouř and E. W. Blanch, *Nature Chem.*, 2015, **7**, 591–596.

194 T. Giovannini, M. Rosa, S. Corni and C. Cappelli, *Nanoscale*, 2019, **11**, 6004–6015.

195 L. Bonatti, G. Gil, T. Giovannini, S. Corni and C. Cappelli, *Front. Chem.*, 2020, **8**, 340.

196 T. Giovannini, L. Bonatti, M. Polini and C. Cappelli, *J. Phys. Chem. Lett.*, 2020, **11**, 7595–7602.